

Chapter V

Manganese (IV)-oxo Species of Non-heme Anionic Ligand: Generation, Characterisation and Reactivity

Abstract

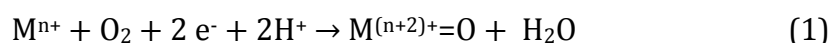
The manganese (III)-(OH) complex, $[(\text{dpaq})\text{Mn}^{\text{III}}(\text{OH})](\text{ClO}_4)$, (**1**) with an anionic N5 non heme ligand H-dpaq (dpaq = 2-[bis(pyridine-2-ylmethyl)]amino-N-quinoli-8-yl-acetamide) has been used to generate a mononuclear manganese (IV)-oxo species, $[(\text{dpaq})\text{Mn}^{\text{IV}}(\text{O})]^+$ (**2**) by proton coupled electron transfer (PCET) process. The manganese (IV)-oxo species (*in situ*) has been characterized by spectral data. The observed EPR and UV-visible spectra of **2** are in close agreement with the simulated spectra based on theoretical calculations. The structure optimization of complex **2** suggests the presence of amidate function *trans* to the oxo moiety in the metal coordination sphere. The theoretical calculations and EPR experiments establish the quartet ground state ($S = 3/2$) of **2**. The Mn^{IV} -oxo species, **2** is capable of activating C-H bonds of deactivated hydrocarbons with low bond dissociation enthalpies (C-H BDEs), such as xanthenes, 9,10-dihydroanthracene (9,10-DHA), 1,4-cyclohexadiene (1,4-CHD) and fluorene. The linear relationship of the normalized second-order rate constant (k_2') with C-H BDEs of the substrates and thermodynamic parameters calculated from Eyring plot shows that the activation of C-H bonds is mediated by hydrogen atom abstraction (HAT) pathway. The species **2** also oxidises thioanisole and *p*-substituted thioanisole to the corresponding sulfoxides following oxygen atom transfer (OAT) from the Mn^{IV} -O species. The electrophilic nature of **2** in the oxygen atom transfer reaction (OAT) of thioanisoles to sulfoxides is established from a high negative Hammett value ($\rho = -2.5$). The complex emerges as the 'most reactive' in comparison to other known $\text{Mn}^{\text{IV/V}}$ -oxo complexes with anionic ligands.

V.1. Introduction

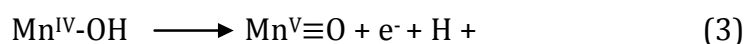
High-valent manganese-oxygen adducts play important roles in diverse biological reactions of several manganese based enzymes [1]. The high-valent manganese-oxo species have been invoked as key intermediates in water oxidation by the oxygen-evolving complex (OEC) of Photosystem II [2]. Spectroscopic and computational studies have also revealed the importance of such species in the oxidized state of manganese-superoxide dismutase (Mn-SOD) [3].

Albeit few, several hydroxo-manganese adducts have also invoked as key intermediates in biology. For instance, in mononuclear nonheme lipoxygenases, hydroxo manganese adducts have been found to be the active species that abstracts hydrogen atom from 1, 4-pentadiene subunits containing fatty acids leading to the formation of alkyl peroxides [4]. However, arguably the most important physiological role played by the hydroxo-manganese species is its involvement in the oxygen evolving complex (OEC) during photosynthesis [2].

In general, formation of oxo-metal transients is accomplished *via* activation of dioxygen through two-electron reduction and protonation (equation 1).



However, an alternative pathway for the generation of oxo-manganese transients has been proposed during water splitting by OEC [5]. In this case, formation of putative Mn^V-oxo is formed by stepwise one-electron oxidations of the corresponding Mn^{III}-OH₂ and Mn^{IV}-OH species (equation 2 and 3).



The abstraction of a hydrogen-atom from a Mn-OH or Mn-OH₂ moiety by a nearby tyrosyl radical, YzO•, has been proposed to form an electrophilic Mn^V-oxo species in OEC [6]. It is believed that nucleophilic attack of water on the electrophilic Mn^V-oxo species is of pivotal importance in O-O bond formation in PS II. Along with manganese, Ca²⁺ also plays an indispensable role in the active site of OEC, although the exact role of Ca²⁺ is not known clearly [7].

In the past few decades, tremendous amount of research impetus has been devoted to mimic the chemistry of oxygen evolving complex (OEC) for the development of suitable solar-driven water oxidation catalysts to generate hydrogen, which is considered to be the cleanest C-neutral source of fuel [8]. In order to achieve this goal, formation of $M^{(n+2)+}=O$ through stepwise oxidations of the corresponding low-valent metal-hydroxo or -aquo complex has attracted increasing attention in recent years. Very recently, Nishida *et al.* have elegantly shown the generation of $[Fe^{IV}(O)(N4Py)]^{2+}$ ($N4Py = N,N$ -bis(2-pyridylmethyl)- N -bis(2-pyridyl)methylamine), *via* electron-transfer oxidation of $[Fe^{III}(OH)(N4Py)]^{2+}$ in acetonitrile (MeCN) in presence of various proton acceptors (PA) and one-electron oxidizing agent $[Ru^{III}(bpy)_3]^{3+}$ [9]. Borovik *et al.* reported a series of monomeric Mn-oxo complexes $[Mn^nH_3buea(O)]^m$ ($n = 3+$ to $5+$; $m = 2-$ to 0) based on a strong anionic ligand $[H_3buea]^{3-}$ ($[H_3buea]^{3-}$, tris[(N' -tert-butylureaylato)- N -ethylene]aminato) [10]. The complexes were prepared starting from the $[Mn^{III}H_3buea(O)]^{2-}$ complex and using ferrocenium ion as the oxidant [10]. Apart from the complexes developed by Borovik *et al.*, high-valent oxo-manganese complexes bearing anionic ligands have been sparsely reported in the literature [11]. However, to the best of our knowledge no report of proton coupled electron transfer (PCET) conversion of the Mn(III)-OH complexes to the corresponding oxo-manganese(IV) species is available..

In the present study, a monomeric Mn^{III} -OH species bearing an anionic N5 ligand H-dpaq (H-dpaq = 2-[bis(pyridin-2-ylmethyl)]amino- N -quinolin-8-yl-acetamide) has been synthesized. The rationale behind the choice of the H-dpaq ligand is its structural similarity with the Bleomycin (BLM). BLM is a non heme amido ligand system which belongs to the glycopeptide antibiotic family and has a strong tendency to inhibit tumour development [12]. Jackson and his co-workers have reported the synthesis of the mononuclear Mn^{III} -OH complex $[(dpaq)Mn^{III}OH]^+$ by the treatment of $[Mn^{II}(dpaq)](OTf)$ with dioxygen in acetonitrile medium at 298 K [13]. Earlier attempt to prepare the $Mn^{IV}=O$ species from the oxygenation of $[(dpaq)Mn^{II}](OTf)$ by dioxygen in presence of PPh_3 met with failure [13].

The present work describes the generation of mononuclear high-valent oxo-manganese (IV) species $[(dpaq)Mn^{IV}(O)]^+$ (**2**) from $[(dpaq)Mn^{III}(OH)]^+$ complex (**1**) by reacting with *m*-chloroperbenzoic acid (*m*-CPBA) in presence of proton acceptors

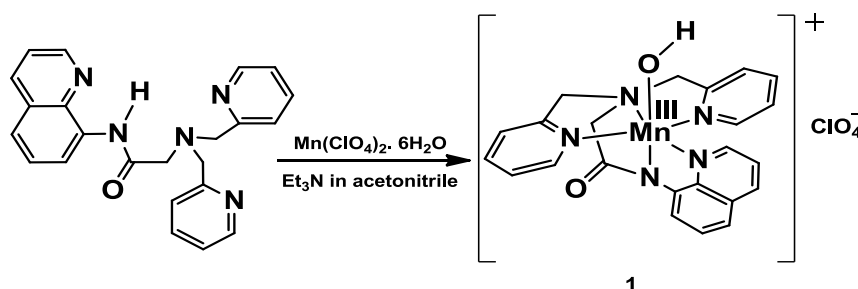
in acetonitrile medium. The high-valent $\text{Mn}^{\text{IV}}\text{-O}$ intermediate has been characterised using different spectroscopic methods. The optimization of probable geometry of **2** has been carried out with the help of density functional theory (DFT) studies.

The reactivity of the species **2** has been investigated for hydrogen atom abstraction (HAT) reaction from weak C-H bond (BDE's in the range of 72 kcal/mol to 78 kcal/mol) and oxygen atom transfer reaction (OAT) for various *p*-substituted thioanisoles. Hammett correlation plot for these *p*-substituted thioanisoles establishes the nature of the intermediate in sulfoxidation reaction.

V.2. Results and discussion

V.2.1. Synthesis and characterization of $[(\text{dpaq})\text{Mn}^{\text{III}}(\text{OH})]^+$ (**1**) complex

The manganese (III)-hydroxo complex $[(\text{dpaq})\text{Mn}^{\text{III}}(\text{OH})](\text{ClO}_4)$, (**1**) has been synthesized involving single step reaction of $\text{Mn}(\text{ClO}_4)_2 \cdot 6\text{H}_2\text{O}$ with H-dpaq in acetonitrile medium at room temperature under aerobic condition, followed by the addition of triethyl amine (Scheme V.1).

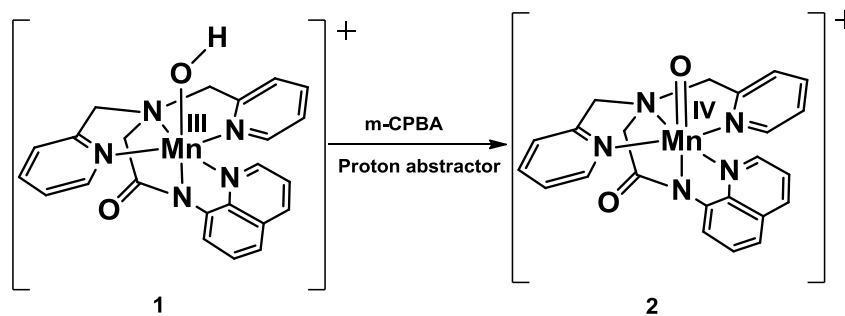


Scheme V.1. Schematic representation of the synthesis of the starting complex, $[(\text{dpaq})\text{Mn}^{\text{III}}(\text{OH})](\text{ClO}_4)$ (**1**).

The complex **1** has been characterized by ESI Mass spectroscopy, where a sharp signal at m/z of 454.07 corresponding to $[(\text{dpaq})\text{Mn}^{\text{III}}(\text{OH})]^+$ is observed (Fig.V.21). Elemental analysis data confirm the formulation of monomeric $\text{Mn}^{\text{III}}\text{-OH}$ complex (calculated: C; 49.86, H; 3.82, N; 12.65, experimental: C; 49.26, H; 3.95, N; 12.47).

V.2.2. Generation of manganese(IV)-oxo complex $[(\text{dpaq})\text{Mn}^{\text{IV}}(\text{O})]^+$ (**2**)

Addition of 1.2 equivalents of *m*-CPBA to a solution of **1** (0.5 mM) containing trifluoromethane sulphonic acid (HOTf, 1.0 equivalent) in acetonitrile results a dark green solution with broad absorptions at 700 nm and 500 nm (shoulder) at 293K (Fig.V.1). Scheme V.2 represents the generation and probable geometry of the $\text{Mn}^{\text{IV}}\text{-O}$ species (**2**).



Scheme V.2. Generation and probable geometry of **2**.

The rate of formation of **2** has been monitored by measuring the change in absorbance at 700 nm with respect to time in kinetics mode. The inset of Fig.V.1, shows the formation of $[(\text{dpaq})\text{Mn}^{\text{IV}}(\text{O})]^+$ (**2**) and thereafter its decay pattern with time at 293 K. Attempts to isolate complex **2** in solid state met with failures.

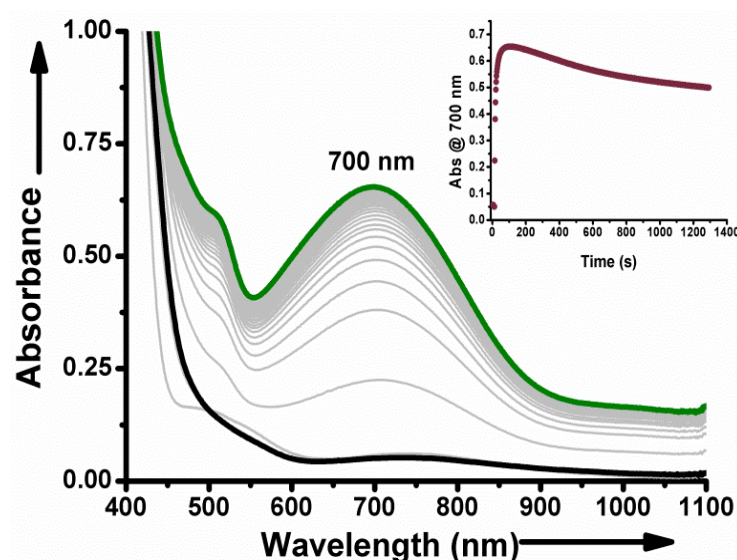


Fig.V.1. Generation of **2** upon the addition of *m*-CPBA (0.6 mM) followed by HOTf (0.5 mM) into **1** (0.5 mM) in Acetonitrile at 293 K. Inset shows the decay pattern of the in situ generated high valent $\text{Mn}^{\text{IV}}(\text{O})$ intermediate **2**.

To get more insight into the role of proton acceptors (PA) in the generation of high valent manganese-oxo species, trifluoromethane sulphonic acid (HOTf) has been replaced by various other PAs such as scandium (III) triflate $[\text{Sc}(\text{OTf})_3]$, perchloric acid (HClO_4), acetic acid (AcOH) and trifluoroacetic acid (TFA) under similar reaction conditions. On addition of *m*-CPBA in presence of $\text{Sc}(\text{OTf})_3$, absorption peaks appears at 500 & 700 nm (dark cyan). Recently, Nam *et al.* has proposed the binding of $\text{Sc}(\text{OTf})_3$ to high-valent oxo-manganese transients [14 a, b]. However, ESI Mass spectrum of **2** excludes such possibilities due to the absence of signals

corresponding to either **(2)**---(Sc³⁺) or **(2)**---(Sc³⁺)₂. The formation of the monomeric high-valent complex **2** in presence of different PAs and *m*-CPBA are shown in Fig.V.2.

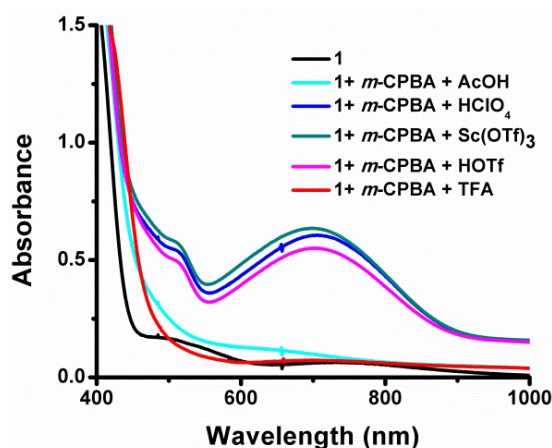


Fig.V.2. Generation of **2** with *m*-CPBA in presence of various PAs ([**1**] 0.5 mM, [*m*-CPBA]: 0.6 mM, [PA]: 0.5 mM).

The addition of HClO₄ instead of HOTf or Sc(OTf)₃ has also resulted in the formation of **2** as shown by blue trace in Fig.V.2. But AcOH or TFA are unable to generate **2** (cyan line and red line respectively).

The oxo-group in **2** may result either from proton abstraction of –O–H bond present in **1** or through oxygen donation by terminal O-donors to metal centre. The reactions have been designed by replacing *m*-CPBA with 1-electron oxidant, [Ru(bpy)₃]³⁺. On addition of [Ru(bpy)₃]³⁺ (1.0 equivalent) to a solution of **1** (0.5 mM) containing 0.5 mM of HOTf resulted in the formation of **2** (red line in Fig.V.3).

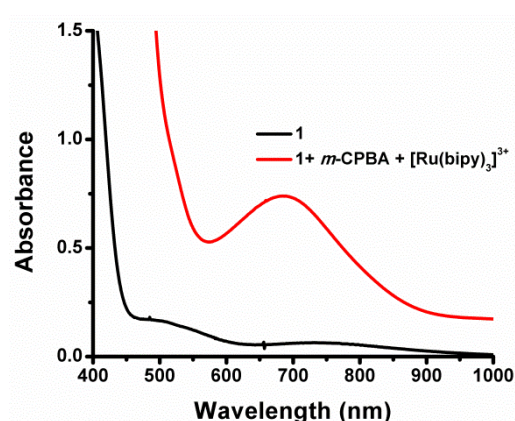


Fig.V.3. Formation of **2** by the addition of [Ru(bpy)₃]³⁺ (0.5 mM) in presence of HOTf (0.5 mM) in acetonitrile at 293 K.

These results suggest PCET-based formation of the [Mn^{IV}(dpaq)(O)]⁺ (**2**) from the corresponding Mn^{III}-OH complex (**1**) in presence of proton acceptor.

The addition of stoichiometric O-donors such as *m*-CPBA (*m*-chloroperbenzoic acid), iodosylarenes, peroxides etc. to complex [(dpaq)Mn^{III}(OH)](ClO₄) (**1**) in acetonitrile fail to produce species **2**. This observation suggests that the presence of a suitable proton acceptor is absolute necessity for the oxidative generation of **2**.

A mixed-valent bis(μ-oxo)dimanganese (III, IV) complex, [(dpaq)Mn^{III}(O)₂Mn^{IV}(dpaq)]⁺ was reported by the reaction of H₂O₂ in presence of trimethylamine, which takes part in electrophilic oxidation of para-substituted 2, 6-di-tert-butyl phenols and nucleophilic aldehyde deformylation of 2-phenyl propionaldehyde (2-PPA) and benzaldehyde [15].

V.2.3. Characterization of the manganese^{IV}-oxo complex [(dpaq)Mn^{IV}(O)]⁺, (**2**)

V.2.3.1. Computational Study

In order to gain further insight into the structural aspects of high-valent Mn^{IV}(O) complex (**2**), the structure shown in Fig.V.4 has been optimized by DFT using the software ORCA (version 4.0) [16]. The molecule is optimized with TPSSh functional [17] and relativistic basis set implemented through zeroth-order regular approximation (ZORA) [18], retaining one-center terms and using ZORA-recontracted def2-TZVP basis sets for all elements other than C and H, for which ZORA-def2-SVP basis sets were used. Increased integration accuracy (Grid6, GridX8 and IntAcc 6.0 in ORCA convention) and tight SCF convergence criteria were applied [19]. To confirm about the ground spin state of the molecule, optimization is performed both on the 3/2 and 1/2 spin state. The quartet spin state is found marginally stable (ca. 5 Kcal mol⁻¹) over the doublet and hence all the subsequent calculations are carried out on the quartet ground spin state. Mulliken spin population indicates Mn (IV) oxidation state with significant spin polarization on O. This is interesting to note that the asymmetry of ligand is translated into the Mn–N equatorial bond lengths as the Mn–N1 bond is significantly shorter than the other Mn–N bonds. This structural asymmetry has major implication in setting the electronic structure and subsequent reactivity. For explanation of the optical absorption, the electronic structure of the complex has been analysed with multiconfigurational self-consistent field theory (MCSCF) implemented through CASSCF/NEVPT2 calculation.

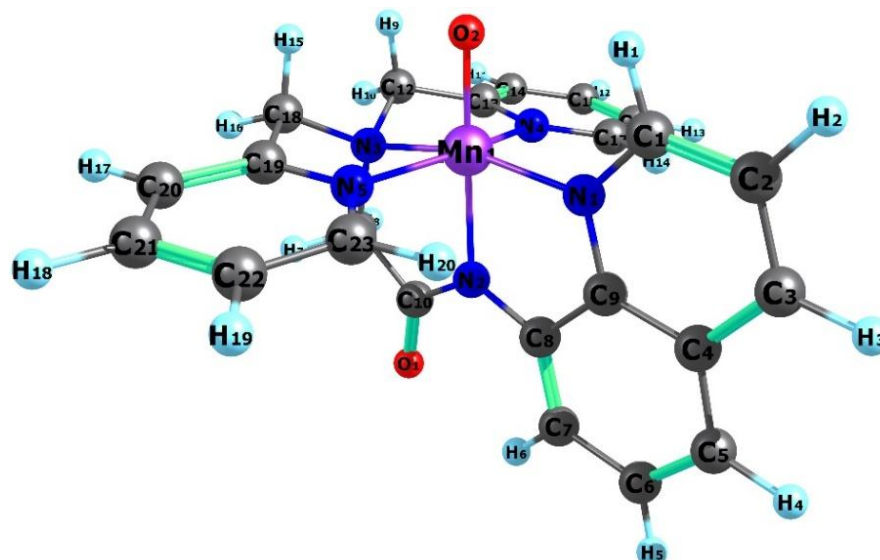


Fig.V.4. DFT-optimized structure of $[\text{Mn}^{\text{IV}}(\text{O})(\text{dpaq})]^+$ (**2**). Purple, Red, Blue, Grey and Cyan colored atoms refer to Mn, O, N, C, and H respectively.

Table V.1. Selective bond distances (\AA) obtained from the optimised structure.

Bonds	Bond Distance (\AA)	Mn spin	O2 spin
Mn - N1	1.99	2.54	0.61
Mn - N2	2.01		
Mn - N3	2.03		
Mn - N4	2.03		
Mn - N5	2.03		
Mn - O	1.69		

For this calculation a active space of 9 electrons in 8 orbitals are used, which include Mn-O σ and π bonding and antibonding orbitals, the nonbonding metal d_{xy} orbital and the σ antibonding orbital ($d_{x^2-y^2}$) between Mn and equatorial nitrogen (Fig.V.5).

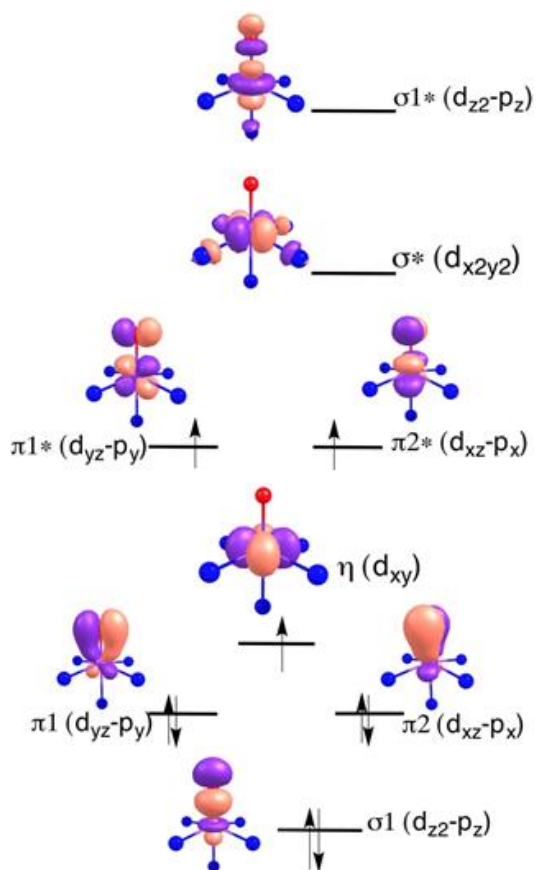


Fig.V.5. MO splitting pattern obtained at CASSCF/NEVPT2 level of theory.

The MO splitting pattern obtained above stands out as an effective guide in explaining of the experimental optical absorption spectra (Fig.V.1). The σ^* orbital is energetically very close to the π^* set of orbitals, which can be attributed to the longer bond length between Mn and equatorial nitrogens compared to strong Mn – O bond. The weak interaction between Mn and equatorial nitrogen stabilizes σ^* orbital minimizing the π^* - σ^* energy gap, which might have major implication towards the reactivity of the system. Though, this can be noticed in Fig.V.6 that the calculated peak positions, particularly in the longer wave length region are downshifted compared to the experiment, major excitations with two closely spaced wavelength range helps to elucidate the origin of experimental absorption bands. The computed wavelength of 572 and 652 nm can be correlated with the experimental 700 nm peak. These absorptions are found to be associated with π_1 , π_2 – η electronic transition. Since, the π MOs are ligand – dominated whereas the η orbital is a non-bonding $d_{x^2-y^2}$ orbital, these transitions can be regarded as the ligand to metal charge transfer (LMCT). Electronic excitation from the doubly occupied π MO (DOMO) to the singly occupied η MO (SOMO) will leave one unpaired electron in

the ligand MO with major contribution from O p_x , p_y orbital leading to oxyl radical character. The second set of transitions occurring at 479 and 499 nm dictates the origin of 500 nm peak in the experimental band. These wave lengths are assigned to $\pi^* - \sigma 1^*$ transitions. However, these d – d transitions being Laporte forbidden should be less intense than the Laporte allowed LMCT, but in the present case the structural asymmetry of the complex helps to gain intensity for such transitions. These transitions are very similar to another similar octahedral $Mn^{IV} - O$ complex [20].

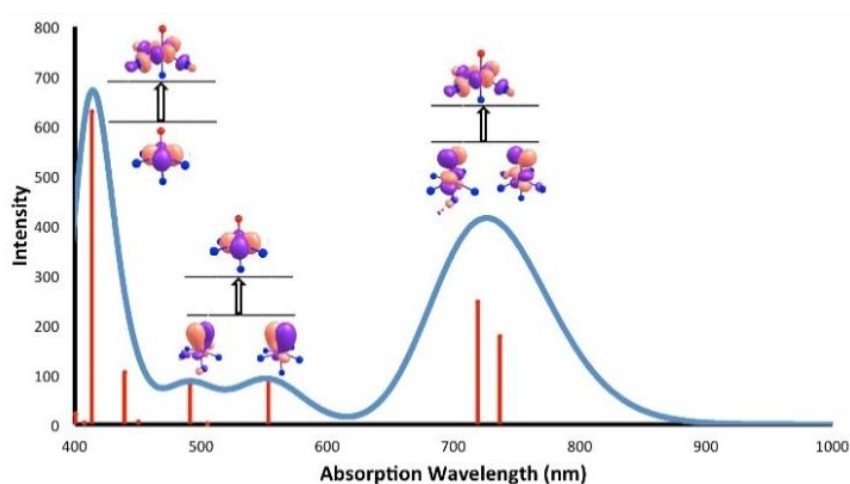


Fig.V.6. Optical absorption spectrum obtained from computation, red sticks imply individual transitions contributing to gaussian peaks.

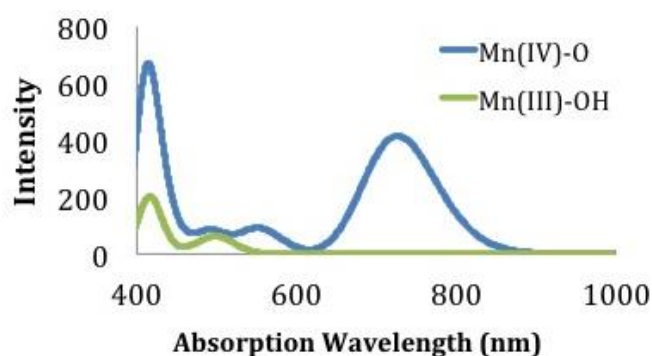


Fig.V.7. Optical absorption spectra of $[(dpaq)Mn^{III}(OH)]ClO_4$ (blue lines) & $[(dpaq)Mn^{IV}(O)]^+$ (**2**, green lines) in acetonitrile obtained by TDDFT calculations.

V.2.3.2. Electron Paramagnetic Resonance Spectrometry

The formation of high valent manganese complex **2** (*in situ*) has been established on the basis of EPR spectroscopy. The acetonitrile solution of complex **2** was frozen at 77 K. The X-band continuous wave EPR spectra of **2** show two signals, one at lower field region with a $g = 4.88$ and the other at high field with $g = 2.088$ (~ 2.1) (Fig.V.8).

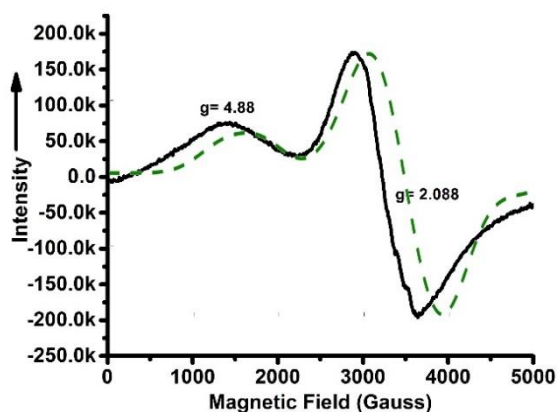


Fig.V.8. Experimental X-band EPR spectrum of **2** (black line) and the simulated EPR spectrum (green line) obtained using Easy Spin.

The feature and complexity of the EPR spectra of a Mn^{IV} system is dependent on the magnitude of the axial zero field splitting parameter D . The EPR spectra of $\text{Mn}(\text{IV})$ centre usually show two signals, one at lower field, i.e., $g = 3-6$ and the another one at higher field with $g = 2$. When $D \gg h\nu$ (the magnitude of applied magnetic field frequency, generally 0.31 cm^{-1}), the signal in the region of $g = 3-6$ is more intense than the signal at $g = 2$. The intensity of signal at $g = 2$ predominates over that of lower field signal when $D \ll h\nu$ (0.31 cm^{-1}) (16a-d). When $D = 0$, no signal at lower frequency appears and the spectrum shows a single sharp band at $g = 2$ [21].

Our system shows higher intensity of the signal at $g = 2.1$ than that at $g = 4.88$, which suggests lower D value compared to 0.31 cm^{-1} .

EPR signal of the given complex is simulated (Fig.III.8) with help of the Easy Spin package [22]. For this simulation, a $|D|$ value of ca. 0.1 cm^{-1} was required along with the rhombicity parameter 0.18. A line-width of 70 mT is used, which averages out the finer splitting of the peaks arising from g -anisotropy and hyperfine coupling constant (A). The first peak at $g \sim 4.9$ arises from $m_s = \pm 3/2$ states and the transition between lower $m_s = \pm 1/2$ states is responsible for the $g \sim 2.09$ signal. Similar EPR transitions have previously been reported for other $S = 3/2$ $\text{Mn}(\text{IV})$ complexes [21 b-d] though precise ground-state spin Hamiltonian parameters have not been reported frequently for mononuclear $\text{Mn}(\text{IV})$ compounds [23].

V.2.3.3. LC mass spectroscopy

The high valent oxo-manganese complex **2** (*in situ*) has been detected with the help of LC-MS analysis. The signal at m/z 453 corresponds to the species $[(\text{dpaq})\text{Mn}^{\text{IV}}(\text{O})]^+$ (Fig.V.9).

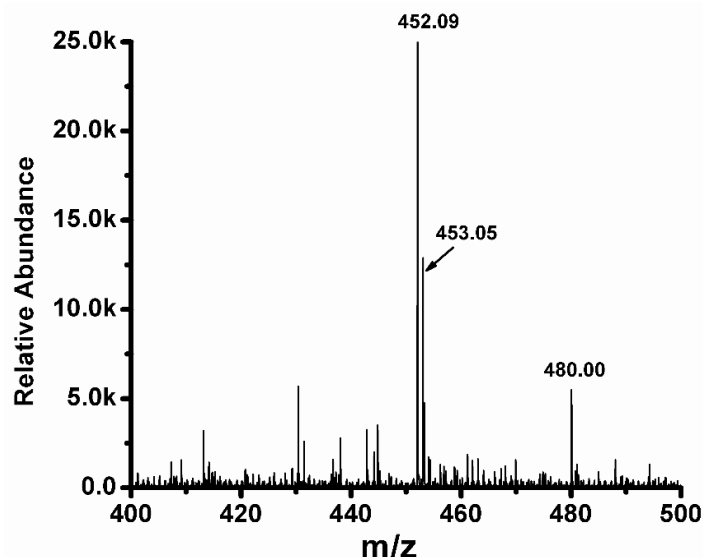


Fig.V.9. LC-MS spectrum of $[(\text{dpaq})\text{Mn}^{\text{IV}}(\text{O})]^+$ (**2**) in acetonitrile.

To investigate the source of O atom bound to the Mn^{IV} center, O^{18} labeling experiments have been designed. Addition of H_2O^{18} to **2** (*in situ*) shows the signals for $[(\text{dpaq})\text{Mn}^{\text{III}}(\text{OH})]^+$ and $[(\text{dpaq})\text{Mn}^{\text{II}}]^+$, but no signal corresponding to $[(\text{dpaq})\text{Mn}^{\text{IV}}(\text{O}^{18})]^+$ (m/z 455) is observed indicating the decay of **2** in presence of water. The reaction between **2** and water has been monitored by UV-visible spectroscopy, which shows rapid decay of absorption band at 700 nm (Fig.V.9).

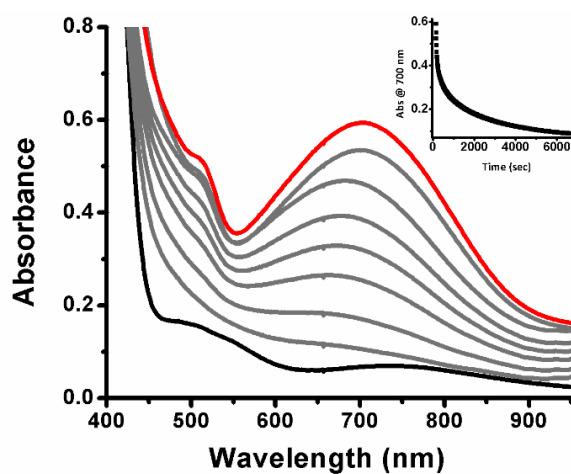


Fig.V.10. Changes in UV-visible spectral changes for **2** upon addition of H_2O (50 mM, 100 equivalents with respect to **2**) at 293 K. Inset shows the decay of the 700 nm after the addition of water *w.r.t* time.

This observation indicates that the $\text{Mn}^{\text{IV}}\text{-O}$ species, **2** reacts with H_2O at a rate faster than its exchange with labeled water.

V.3. Reactivity of **2** with hydrocarbons

Kinetic measurements have been undertaken to elucidate the reactivity of **2** with hydrocarbons having weak C-H bond dissociation energy (C-H BDE). The reaction kinetics has been monitored by measuring the rate of decrease in absorbance at 700 nm with respect to time using UV-visible spectrophotometer. The species **2** reacts with deactivated hydrocarbons, such as xanthene, 1,4-cyclohexadiene (1,4-CHD), 9,10-dihydroanthracene (9,10-DHA), fluorine (BDE_{C-HS} range from 75.5 to 80 Kcal Mol⁻¹) following a pseudo first order reaction kinetics. The value of second order rate constant, ' k_2 ' (in $\text{M}^{-1} \text{S}^{-1}$) for each substrate has been determined from the slope obtained from a linear plot of pseudo first order rate constant (k_{obs}) vs. substrate concentration at 293 K.

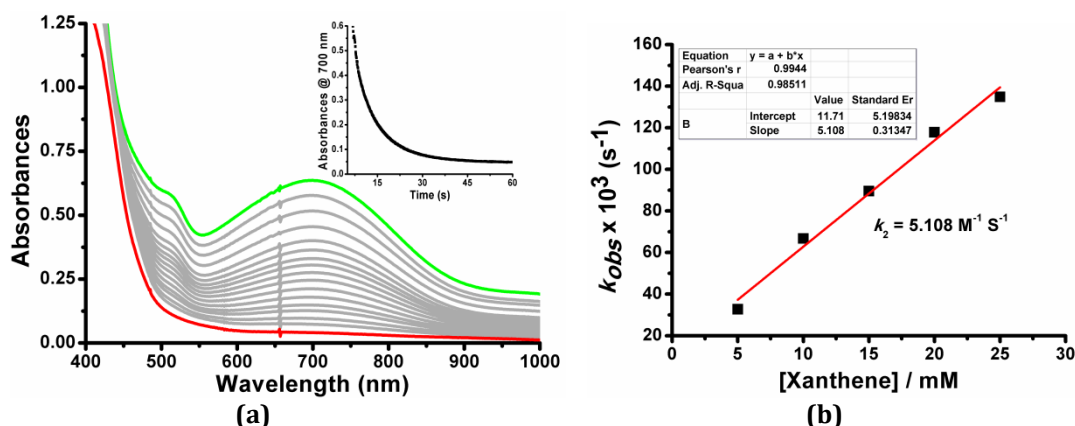


Fig.V.11. (a) Changes in UV-visible spectral changes for **2** upon addition of 50 equivalents of xanthene at 293 K. Inset shows the pseudo first order decay pattern of **2** after addition of xanthenes; **(b)** plot of k_{obs} (s^{-1}) against substrate concentration (in mM) to determine second order rate constant, k_2 ($\text{M}^{-1} \text{s}^{-1}$) for xanthenes.

In case of xanthenes having C-H BDE = 75.5, the second order rate constant (k_2) is found to be $5.1 \text{ M}^{-1}\text{s}^{-1}$ (Fig.V.11) showing high reactivity of **2**. The second order reaction rates for other substrates with low C-H BDEs are given in table V.2.

Table V.2. C-H bond dissociation enthalpies (BDE_{C-H}) and k'_2 values for the reaction of **2** with various substrates at 293 K.

Entry	Substrate	BDE_{C-H} s (kcal mol ⁻¹)	k_2 (M ⁻¹ s ⁻¹)
1	Xanthene	75.5	5.1
2	9,10-DHA	77	3.68
3	1,4-CHD	78	0.216
4	Fluorene	80	0.115

V.3.1. Reactivity with 9,10-dihydro anthracene (9,10-DHA)

The species **2** is capable of oxidising 9,10-dihydroanthracene (9,10-DHA) to anthracene (60% yield) as a sole product, which indicates hydrogen atom abstraction (HAT) from the substrate. The decay of **2** is remarkably faster after addition of 5 equivalents of 9,10-DHA to a solution of **2** (0.5 mM, *in situ*) at 293 K (Fig.V.12). The second order rate constant (k_2) value for the HAT reaction from 9,10-DHA has been calculated to be 3.68 M⁻¹ s⁻¹, which is almost 10 times higher than that reported for [(BQCN)Mn^{IV}(O)(OH₂)₂]²⁺ ($k_2 = 1.2 \times 10^{-1}$ M⁻¹ s⁻¹) [24].

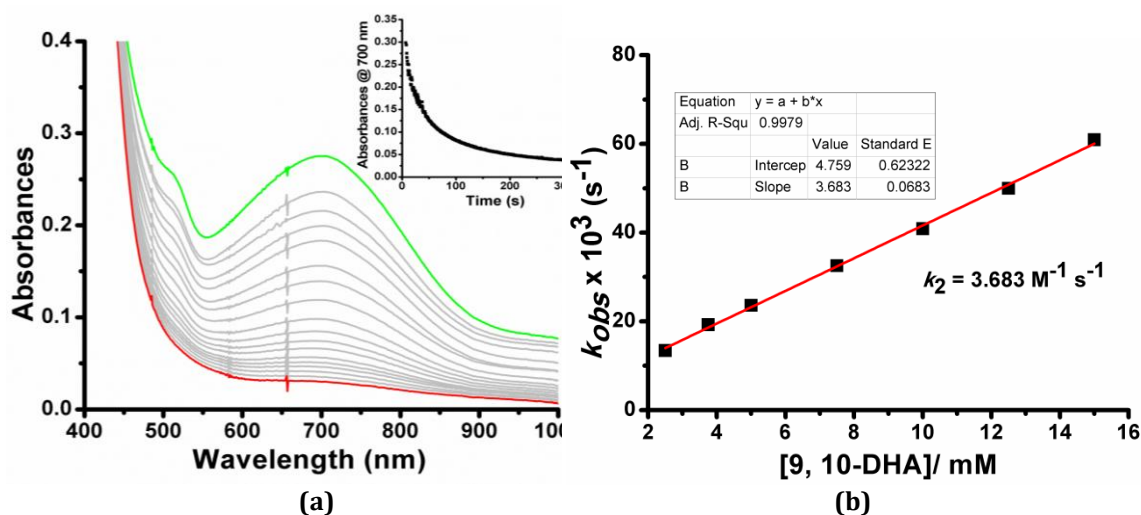


Fig.V.12. (a) Changes in UV-visible spectra of **2** upon addition of 20 equivalents of 9,10-DHA at 293 K. The inset shows the decay pattern of **2** after addition of 9,10-DHA; (b) plot of k_{obs} (S⁻¹) against substrate concentration (in mM) for the determination of second order rate constant (k_2 in M⁻¹ S⁻¹) for 9,10-DHA.

The solution obtained after complete decay of **2** was passed through a silica gel column and the final product was collected. The UV-visible spectrum of the product confirms the generation of anthracene with 60% yield. The GC MS analysis shows that anthracene is the sole product.

V.3.2. Reactivity with 1,4-cyclohexadiene (1,4-CHD)

The hydrogen atom abstraction reaction (HAT) reaction of **2** with 1,4-CHD gives benzene (70% yield) with second order rate constant (k_2) of $5.14 \times 10^{-1} \text{ M}^{-1} \text{ s}^{-1}$ (Fig.V.13). The reactivity of **2** with 1,4-CHD is quite straight forward unlike the reported reactivity of $[(\text{MePyTACN})\text{Mn}^{\text{IV}}(\text{O})(\text{OH})]^+$ ($k_2 = 1.9 \text{ M}^{-1} \text{ s}^{-1}$) [25] but it is comparable with that of $[(\text{BQCN})\text{Mn}^{\text{IV}}(\text{O})(\text{OH}_2)]^{2+}$ ($k_2 = 7.6 \times 10^{-2} \text{ M}^{-1} \text{ s}^{-1}$) reported in literature [24]. The HAT reaction of **2** with 1,4-CHD is almost six times faster than that of $[(\text{N4Py})\text{Mn}^{\text{IV}}(\text{O})(\text{HOTf})_2]^{2+}$ ($0.92 \times 10^{-1} \text{ M}^{-1} \text{ s}^{-1}$) [14b], but a higher value of k_2 was reported earlier in the case of $[(\text{N4Py})\text{Mn}^{\text{IV}}(\text{O})]^{2+}$ ($k_2 = 6.2 \text{ M}^{-1} \text{ s}^{-1}$ at 298 K) [26].

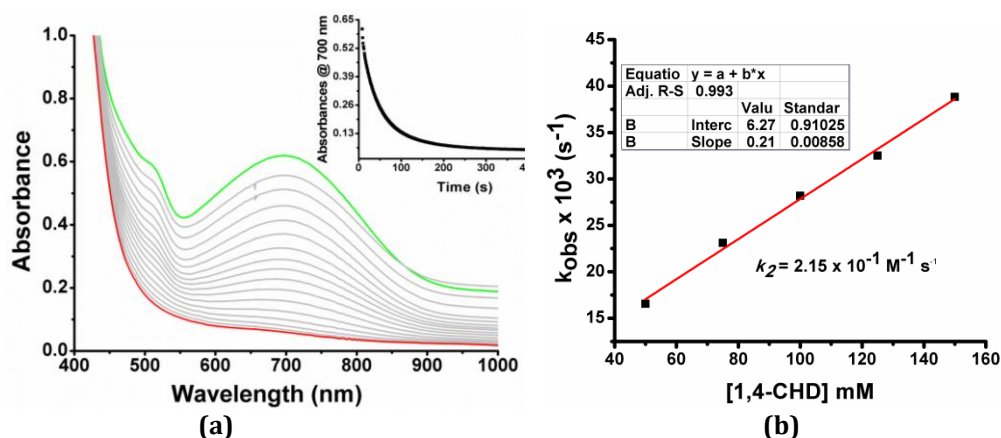


Fig.V.13. (a) Changes in the UV-visible spectra of **2** after the addition of 100 equivalents of 1, 4-CHD at 293 K. Inset picture represents the decay pattern of **2** after the addition of 1, 4-CHD; (b) plot of k_{obs} (S^{-1}) against substrate concentration (mM) for the determination of second order rate constant, k_2 ($\text{M}^{-1} \text{ s}^{-1}$) for 1, 4-CHD.

On the otherhand a two Sc^{3+} ion bound complex of $[(\text{N4Py})\text{Mn}^{\text{IV}}(\text{O})]^{2+}$ shows lower k_2 ($0.035 \text{ M}^{-1} \text{ s}^{-1}$) than that of **2** [14a].

The reactivity of **2** with the hydrocarbons having weak C-H bonds is either comparable or much higher than previously reported systems (Table V.3).

Table V.3. Second-order rate constants (k_2) for oxidation reactions of Oxomanganese complexes.

Complex	k_2 ($\text{M}^{-1} \text{ s}^{-1}$)			Ref
	Xanthene	9,10-DHA	1,4-CHD	
$[(\text{dpaq})\text{Mn}^{\text{IV}}(\text{O})]^+$	5.1 (20°C)	3.92 (20°C)	0.216 (20°C)	This work
$[(\text{N4Py})\text{Mn}^{\text{IV}}(\text{O})]^{2+}$	-	8.9 (25°C)	6.2 (25°C)	26
$[\text{Mn}^{\text{IV}}(\text{O})(\text{N4Py})]^{2+} \cdot \text{Sc}^{3+}$	-	-	1.2 (25°C)	14a
$[\text{Mn}^{\text{IV}}(\text{O})(\text{N4Py})]^{2+} \cdot 2\text{Sc}^{3+}$	-	-	0.035 (0°C)	14a
$[(\text{N4Py})\text{Mn}^{\text{IV}}(\text{O})]^{2+} (\text{HOTf})_2$	-	-	0.92 (25°C)	14b
$[\text{Mn}^{\text{IV}}\text{H3buea}(\text{O})]^-$	-	0.026 (20°C)	-	11d
$[\text{Mn}^{\text{III}}\text{H3buea}(\text{O})]^{2-}$	-	0.48 (20°C)	-	11d
$[\text{Mn}^{\text{IV}}(\text{Me}_2\text{EBC})(\text{O})^2]$	0.048 (15°C)	0.01496 (15°C)	0.0159 (15°C)	27

The plot of $\log k'_2$ values against the corresponding C-H bond dissociation energies (BDEs) of the substrates show a linear fitting as represented by Fig.V.14.

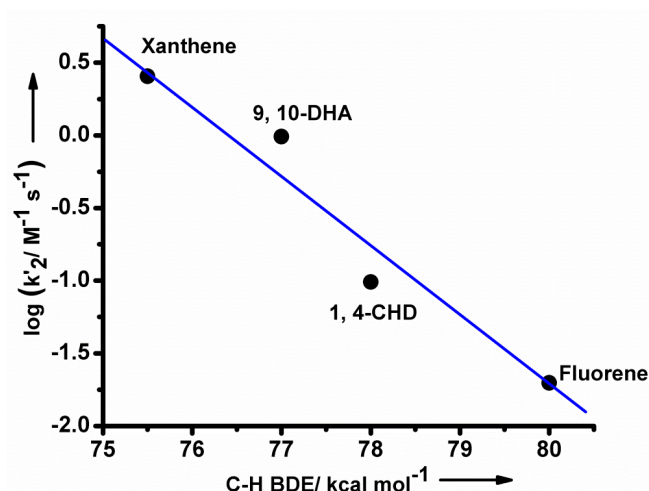


Fig.V.14. Plot of $\log(k'_2)$ of **2** vs. the C-H BDE of substrates (BDE of substrates; Xanthene: 75.5 kcal mol⁻¹, 9, 10-DHA: 77 kcal mol⁻¹, 1, 4-CHD: 78 kcal mol⁻¹, fluorene: 80 kcal mol⁻¹).

The normalized second-order rate constants, k'_2 ($k'_2 = k_2/\text{number of equivalent target C-H bonds}$) measured for the reactions of **2** with the substrates, were plotted as a function of C-H bond dissociation energy (C-H BDE) (number of equivalent target C-H bonds for Xanthene = 4; 9, 10-DHA = 4; 1, 4-CHD and fluorene = 2 respectively). A linear correlation between the reaction rate and C-H bond dissociation energy of the substrates was obtained, indicating H-atom abstraction by **2** is the rate-determining step in the C-H bond activation reaction.

The thermodynamic parameters have been calculated from Eyring plot within a range of temperature from 293 K to 308 K (Fig.V.15.).

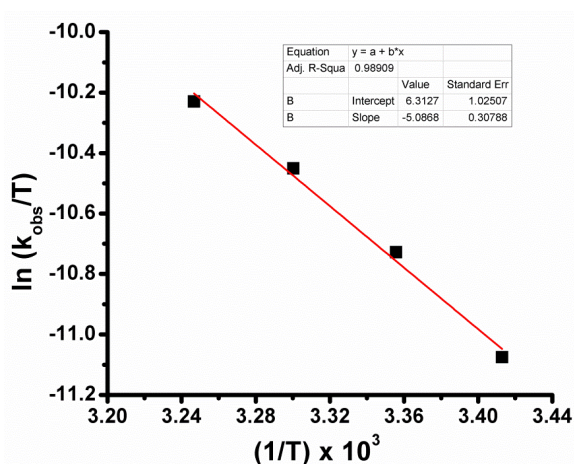


Fig.V.15. Eyring plot of $\ln(k_{\text{obs}}/T)$ vs. $1/T$ calculated from 1, 4-CHD (100 equivalents with respect to 0.5 mM **2**).

From the slope of the plot ΔH^\ddagger has been calculated to be $10.36 \text{ kcal K}^{-1} \text{ mol}^{-1}$, and ΔS^\ddagger is found to be $-36.3 \text{ cal mol}^{-1}$ as calculated from the intercept. From these values ΔG^\ddagger at 298 K has been calculated to be $20.38 \text{ kcal mol}^{-1}$. The calculated thermodynamic parameters are well in agreement with that of a PCET driven HAT reaction.

V.4. Reactivity of **2** in Oxygen Atom Transfer (OAT) reaction

The reaction of **2** with thioanisole and substituted thioanisoles follows OAT pathway and yields corresponding sulfoxides. The reaction kinetics have been monitored by UV-visible spectroscopy. On addition of thioanisole to the complex **2** (*in situ*) in acetonitrile, the absorption peak at 700 nm rapidly decreases with time at 293 K (Fig.V.16). The inset in Fig.V.16 shows the decay pattern of **2** upon addition of thioanisole. The reaction of **2** with thioanisole is so fast that the second order rate constant for sulphur oxidation could not be obtained.

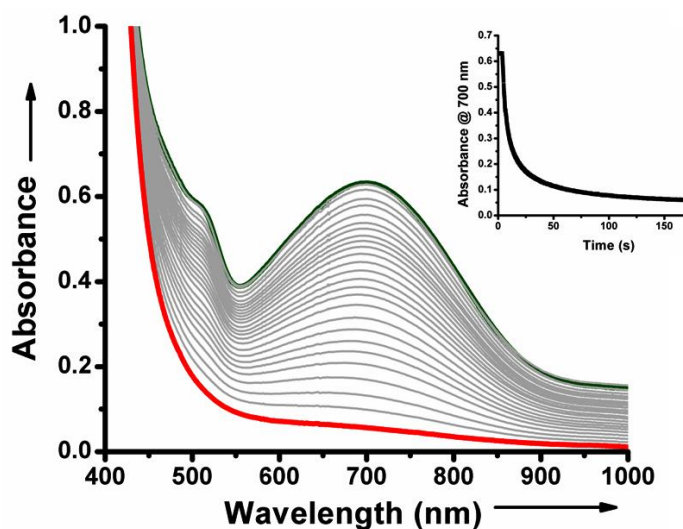


Fig.V.16. Spectroscopic change of **2** upon addition of 10 equivalents of thioanisole (**1**: 0.5 mM, $\text{Sc}(\text{OTf})_3$: 0.5 mM and *m*-CPBA: 0.6 mM) in Acetonitrile solution at 293 K. inset shows the pseudo first order decay pattern of **2** upon addition of thioanisole under the same reaction condition.

The second order rate constant, k_2 , for sulphur oxidation reactions, has been determined by reacting *p*-nitrothioanisole with **2** at 293 K and the decay of the Mn(IV)-oxo species was monitored by UV-visible spectrophotometer. From the plot of k_{obs} versus substrate concentration, k_2 is evaluated to be $5.0 \times 10^{-2} \text{ M}^{-1} \text{ s}^{-1}$ at 293 K (Fig.V.17).

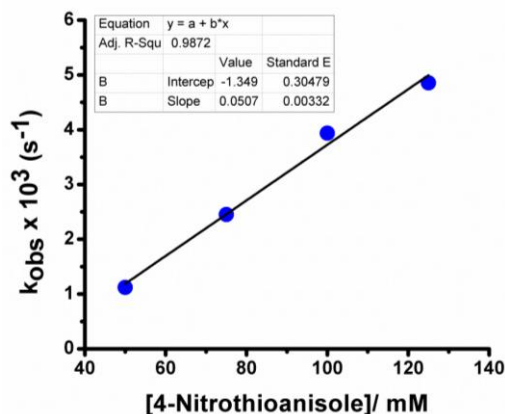


Fig.V.17. Plot of k_{obs} (s^{-1}) against the concentration of 4-nitrothioanisole (in mM) to determine the second order rate constant (k_2 in $\text{M}^{-1}\text{s}^{-1}$) for sulphur oxidation at 293 K.

The high reactivity of **2** with thioanisole and substituted thioanisole is well established from linear correlation of Hammett plot. The basic Hammett equation is

$$\log (K/K_0) = \sigma_p \cdot \rho \dots\dots\dots(i)$$

Where ' K ' is the equilibrium constant for a given equilibrium reaction with substituent X at 4 or *para*-position of the benzene ring and the reference ' K_0 ' is the same when the substrate is X is H atom at *para*-position to the substituent. The value of ' σ_p ' depends only on the specific substituent, X and ' ρ ' on the type of reaction not on the nature of X. The equation also holds for reaction rates ' k ' of a number of reactions with substituted benzene derivatives and becomes

$$\log (k/k_H) = \sigma_p \cdot \rho$$

$$\text{or, } \log (k_{\text{rel}}) = \sigma_p \cdot \rho \dots\dots\dots(ii)$$

In this relation ' k_H ' is the reaction rate of unsubstituted substrate, i. e., thioanisole and ' k ', that of *para*-substituted thioanisoles. The plot of $\log (k_{\text{rel}})$ against ' σ_p ' values of *para*-substituted thioanisoles gives a straight line with a slope of -2.478 (Fig.V.18).

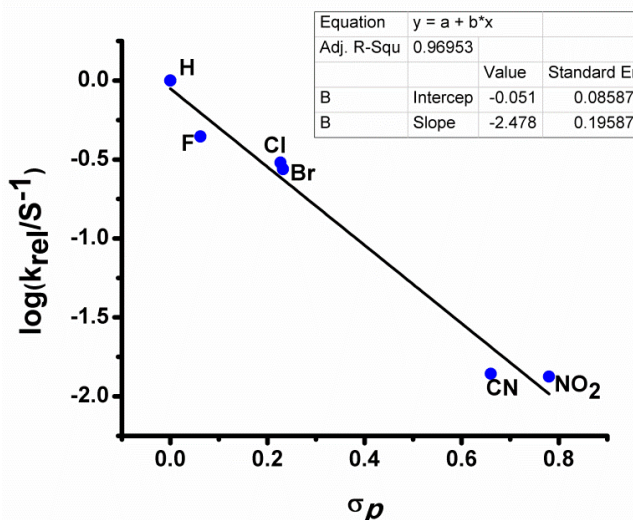


Fig.V.18. Hammett plot of $\log k_{\text{rel}}$ against σ_p of *p*-substituted thioanisoles for **2** (0.5 mM with $\rho = -2.478$ in Acetonitrile at 293 K).

The value of slope stands for ρ , which is negative and indicates the sulphur oxidation reaction accomplished by **2** is electrophilic in nature. The product in sulphur oxidation of thioanisole has been quantified by NMR spectroscopic method and found to be 30% conversion to methyl phenyl sulfoxide with no other oxidised products like sulfone.

V.5. Conclusion

1. A mononuclear nonheme intermediate, **2** $[(\text{dpaq})\text{Mn}^{\text{IV}}(\text{O})]^+$ was generated by the reaction of $[(\text{dpaq})\text{Mn}^{\text{III}}(\text{OH})](\text{ClO}_4)$ with *m*-CPBA in presence of $\text{Sc}(\text{OTf})_3$ in acetonitrile.

To the best of our knowledge this is the first monomeric Mn^{IV} -oxo intermediate generated from a mononuclear manganese(III)-OH complex of a pentadentate N5 carboxamido ligand.

2. The Mn^{IV} -O species **2** cannot be generated in absence of a proton acceptor. This suggests that the formation of the $[\text{Mn}^{\text{IV}}(\text{dpaq})(\text{O})]^+$ (**2**) from the corresponding Mn(III)-hydroxo complex (**1**) is based on proton coupled electron transfer.

3. The Mn^{IV} -O species has been identified on the basis of a signal at m/z 453.05 in LC mass spectrum.

4. The generation of Mn^{IV} centre in **2** was further established by EPR spectroscopy. The X-band continuous wave EPR spectra of **2** in acetonitrile show two signals, one at lower field region with a $g=4.88$ and the other at high field with $g = 2.088$. The

higher intensity of the signal at $g = 2.88$ in experimental and simulated EPR spectroscopic results show lower axial zero field splitting parameter (D) compared to the applied magnetic field frequency (0.31 cm^{-1}).

5. The simulated EPR spectra and TD-DFT calculations establish the quartet ground state ($S = 3/2$) is marginally stable compared to the doublet state ($1/2$) of **2**.

6. The oxo-manganese (IV) complex (**2**) exhibits excellent reactivity in hydrogen atom abstraction (HAT) reactions. The HAT reactivity of **2** has been found to be comparable with the other most reactive oxo-manganese (IV) complexes reported so far. Moreover, the complex exhibits the highest reactivity among the reported non heme $\text{Mn}^{\text{IV}}\text{-O}$ complexes with anionic ligands.

7. The complex **2** also shows reactivity in oxygen atom transfer reactions (OAT) with thioanisole and *p*-substituted thioanisoles. A negative ρ value (-2.5) in the Hammett plot for *p*-substituted thioanisoles, shows the electrophilic nature of the $\text{Mn}^{\text{IV}}\text{-O}$ species in oxidation of thioanisoles.

V.6. Experimental

V.6.1. Materials and Method

Bromoacetyl bromide, 8-amino quinoline and bis-(2-pyridylmethyl)amine were bought from Sigma Aldrich. The oxidant *m*-CPBA was obtained from Fluka chemicals. Trifluoromethanesulphonic acid (triflic acid, HOTf) was purchased from Sigma Aldrich. Xanthene, 9,10-dihydroanthracene (9,10-DHA), 1,4-cyclohexadiene (1,4-CHD), flourene, thioanisole and *p*-substituted thioanisoles were procured from Sigma Aldrich. All the solvents were used of spectroscopic grade and used as obtained without any further purification unless stated otherwise. The UV-visible spectral experiments and kinetic measurements were performed by Agilent 8453 UV-visible spectrophotometer. Electrospray ionization mass spectra were recorded with a Waters QTOF Micro YA263 instrument. X-band EPR measurements were performed by a JEOL JES-FA 200 instrument.

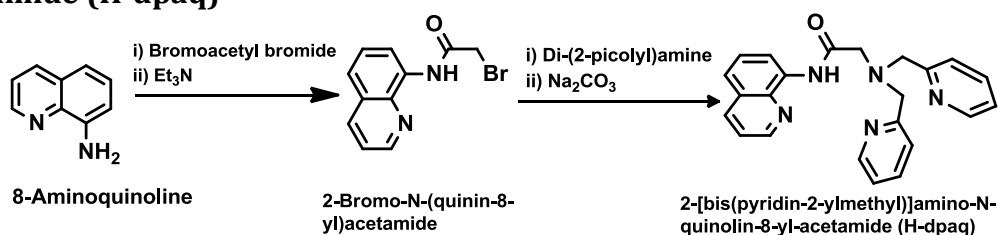
V.6.2. Synthesis of 2-[bis(pyridin-2-ylmethyl)]amino-*N*-quinolin-8-yl-acetamide (H-dpaq) and its Mn^{III}OH complex

V.6.2.1. Synthesis of 2-bromo-*N*-(quinolin-8-yl)acetamide

2-Bromo-*N*-(quinolin-8-yl)acetamide was synthesised by following a reported procedure [28]. 8-Amino quinoline (1g, 0.678 mmol) was dissolved in acetonitrile (40 mL) at 0 °C. A solution of triethyl amine (0.5 mL, 0.8mmol) in acetonitrile (5mL) was added drop wise with stirring at 0 °C over 5 min. To this stirred solution bromo acetyl bromide (0.8 g, 0.68 mmol) dissolved in dichloromethane (10 mL) was added dropwise over a period of 20 min. After 30 min, the reaction mixture was brought to room temperature and the stirring continued for another 2 h. Thereafter, the reaction mixture was passed through a Celite bed. After complete removal of the solvent, the crude product was purified by column chromatography on silica gel (mesh 60-120) using petroleum ether-ethyl acetate (0-6:1 ratio) as eluant affording a light yellow solid. The spectral data of this compound were in full agreement with the earlier reported data.

FT IR in KBr (ν in cm^{-1}): 3208 (s), 3060 (w), 2995 (s), 2939 (ms), 2362 (w), 1670 (s), 1629 (ms), 1594 (s), 1551 (s), 1496 (s), 1454 (w), 1399 (w), 1295 (s), 1234 (s), 1217 (s), 1148 (w), 1038 (w), 897 (ms), 830 (s), 786 (w), 771 (s), 703 (ms), 658 (mw), 614 (w), 583 (ms), 523 (ms), 445 (w), 463 (w), 412 (ms).

V.6.2.2. Synthesis of 2-[Bis(pyridin-2-ylmethyl)]amino-*N*-quinolin-8-yl-acetamide (H-dpaq)



Scheme V.3. Schematic representation of the synthetic route to pentadentate amido ligand 2-[bis(pyridin-2-ylmethyl)]amino-*N*-quinolin-8-yl-acetamide (H-dpaq).

To a degassed solution of 2-Bromo-*N*-(quinolin-8-yl)acetamide (0.9 g, 1.25 mmol, in 100 mL acetonitrile), solid Na₂CO₃ (0.320 g 4 mmol), was added in small portions and the mixture was stirred at 0 °C for 5 min. To this stirred mixture di-(2-picolyl)amine (0.95 mL, 1.35 mmol) dissolved in acetonitrile (10 mL) was added drop wise under the same condition. The reaction was continued for 30 h after

which the colour of the reaction mixture turned pink. The reaction mixture was filtered through a Celite bed and the solvent was removed under vacuo. The pink oil was washed with water repeatedly for complete removal of unreacted Na_2CO_3 and the crude product was extracted into dichloro methane (3x100 mL). The organic layer was evaporated off and the crude brown oil was purified by column chromatography on active neutral alumina (Brockmann activity-II, Merck) using hexane-ethyl acetate (1:1) as eluant. The collected fraction was evaporated to dryness to give a light brown solid. Yield of the product 980 mg, 86%. The product was characterised by ^1H NMR, ESI MS, CHN analysis and FT IR methods. ESI MS : m/z 406 ($\text{M}+\text{Na}^+$), ^1H NMR (500 MHz, CDCl_3): δ 3.542 (s, $-\text{CH}_2\text{CO}-$, 2H), 4.02 (s, $-\text{CH}_2\text{Py}$, 4H), 7.134 (dd, Py5, 2H), 7.501-7.568 (m, Qu3, Qu5, Qu7, 3H), 7.64 (ddd, Py4, 2H), 7.97 (d, Py3, 2H), 8.184-8.189 (dd, Qu4, 1H), 8.51 (d, Py6, 2H), 8.76 (dd, $J = 2.6$ Hz, $J = 6.0$ Hz, Qu6, 1H), 8.93 (dd, 1H), 11.6 (s, $-\text{NHQu}$, 1H). Anal. Calcd for $\text{C}_{23}\text{H}_{21}\text{N}_5\text{O}$: C, 72.04; H, 5.52; N, 18.26. Found: C, 72.25; H, 5.45; N, 18.36.

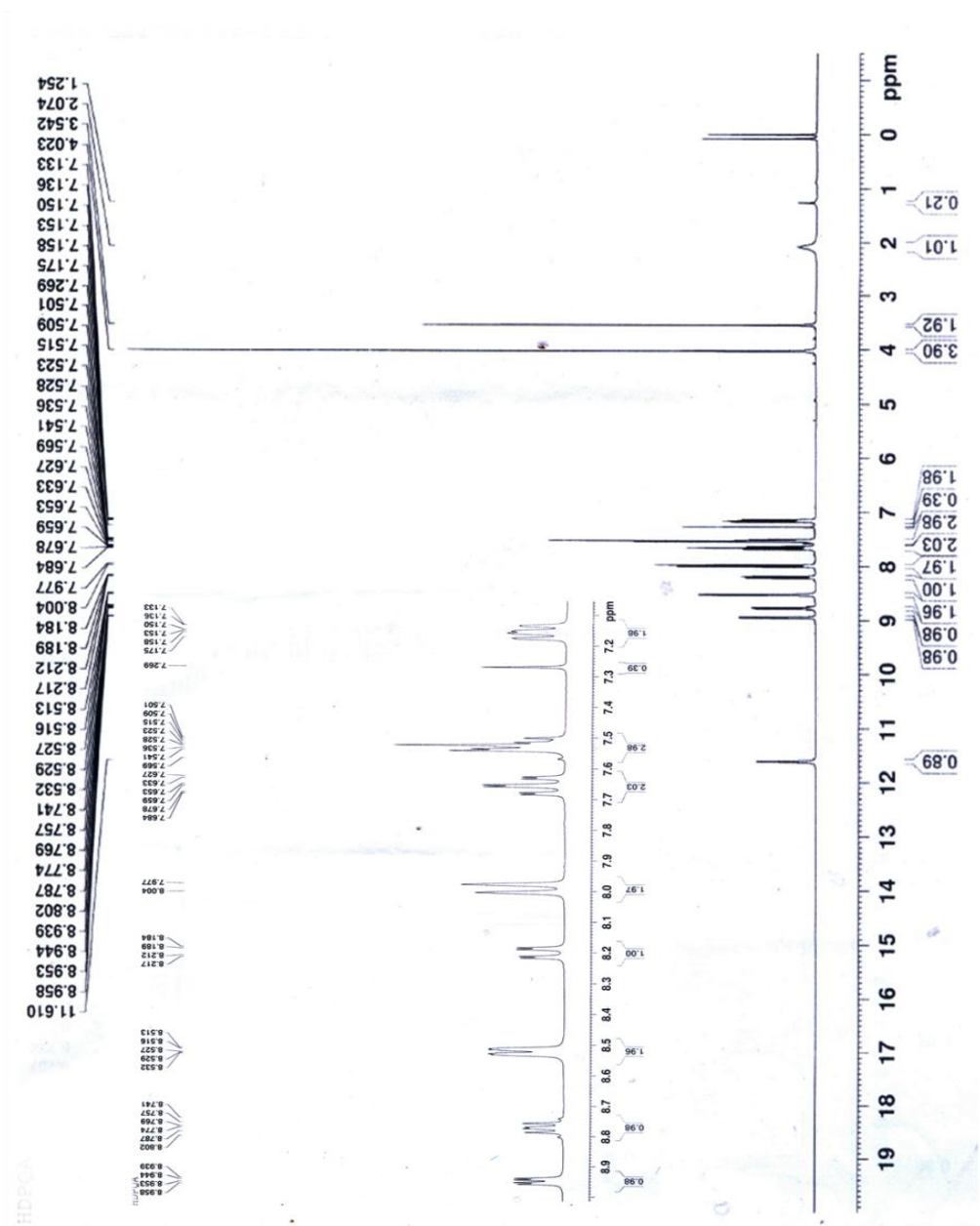


Fig.V.19. Full range ^1H NMR spectra of H-dpaq in CDCl_3 ; the inset shows the expanded aromatic region in the ^1H NMR spectra of H-dpaq in CDCl_3 using TMS as internal standard.

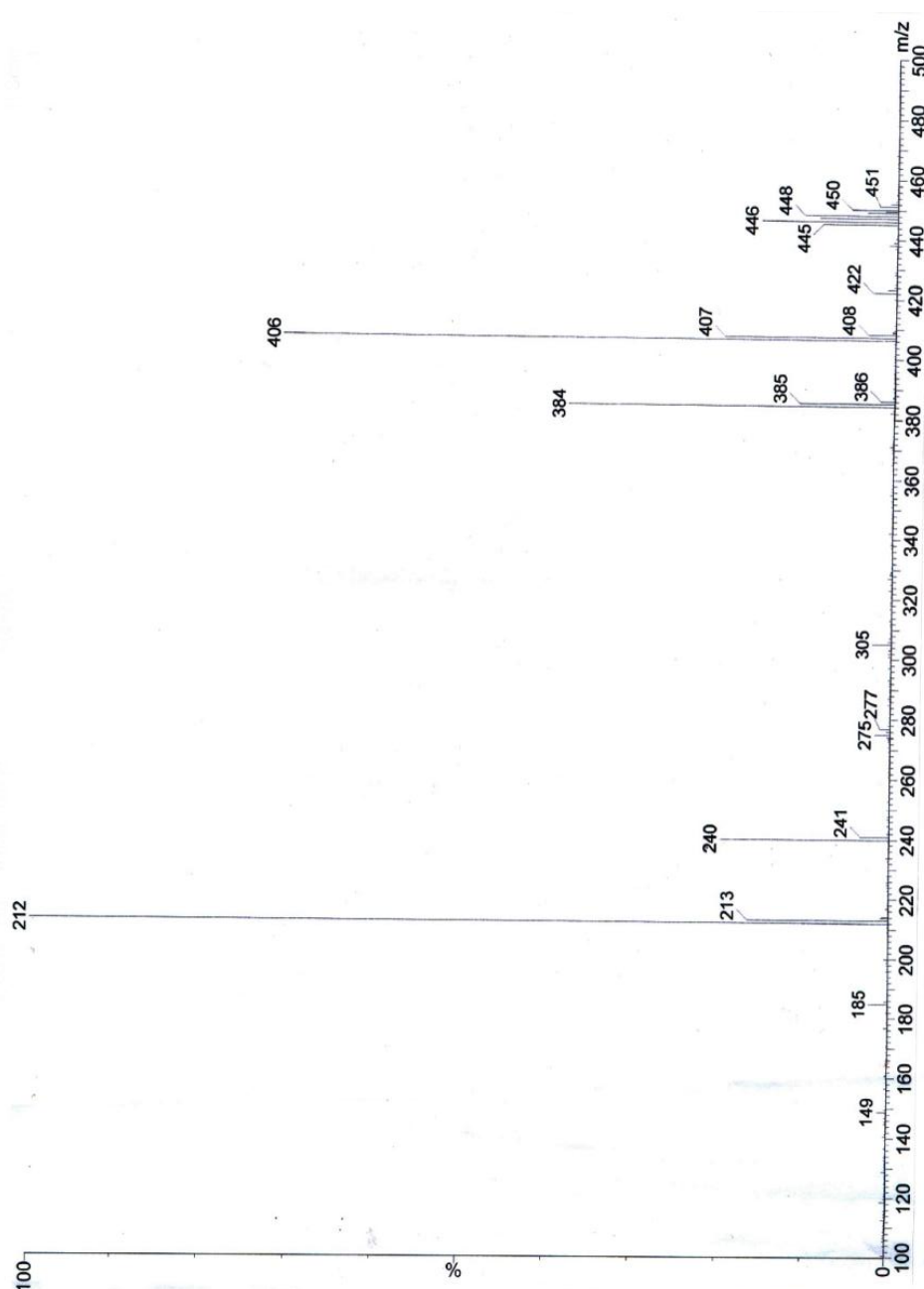


Fig.V.20. ESI Mass spectra of H-dpaq in dichloromethane.

V.6.2.3. Synthesis of $[\text{Mn}^{\text{III}}(\text{OH})(\text{dpaq})](\text{ClO}_4)$ (1)

To a solution of H-dpaq (0.382 g, 1 mmol) in CH_3CN (2 mL), a solution of $\text{Mn}(\text{ClO}_4)_2 \cdot 6\text{H}_2\text{O}$ (0.361 g, 1 mmol) in CH_3CN (1 mL) was added at room temperature, followed by the drop wise addition of triethylamine (1 mmol). The mixture was stirred for 2 h. The light beige colored precipitate was collected and washed with diethyl ether followed by drying in vacuum. The beige colored solid was then dissolved in acetonitrile and stirred in presence of air to give a dark brown solution and dried in vacuum yielding a dark brown solid. Yield: 0.450 g (81%). The

dark brown solid product was characterized by UV-visible spectrophotometer, ESI Mass spectrometry and elemental analysis. UV/visible (CH₃CN): λ_{\max} [nm] (ϵ in M⁻¹cm⁻¹): 486 (252), 743 (108); ESI MS: m/z 454.04; Anal. Calcd: C 49.97, H 3.82, N 12.67 found C 49.26, H 3.95, N 12.47.

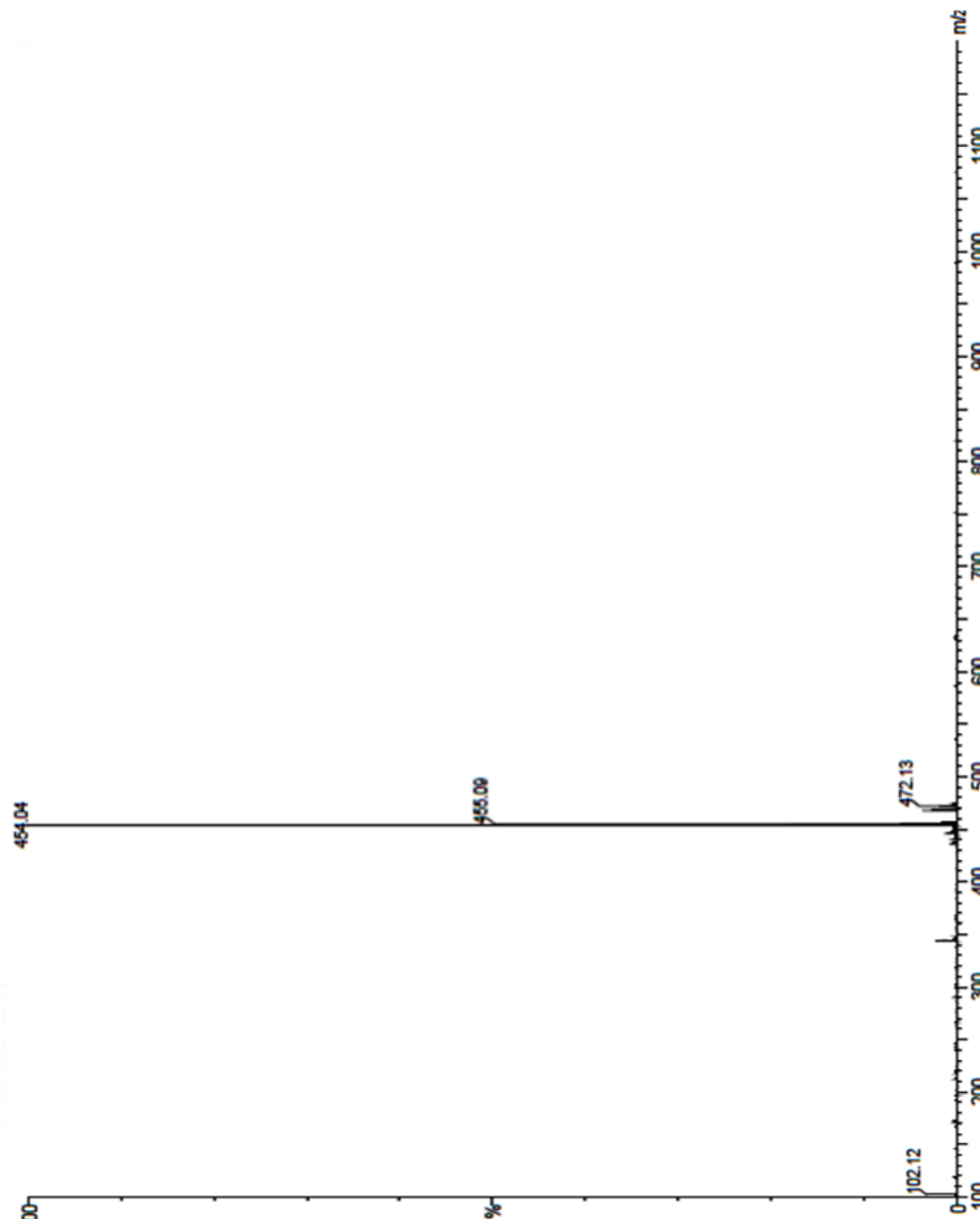


Fig.V.21. ESI-MS spectrum of [(dpaq)Mn^{III}(OH)]ClO₄ (**1**) in acetonitrile. The peak at m/z 454.04 corresponds to [(dpaq)Mn^{III}(OH)]⁺.

V.6.2.4. Preparation of [Mn^{IV}(O)(dpaq)]⁺ (**2**)

[Mn^{IV}(O)(dpaq)]⁺ (**2**) was formed by reacting a 0.5 mM [Mn^{III}(OH)(dpaq)](ClO₄) (**1**) in acetonitrile at 293K with 0.6 mM *m*-CPBA (1.2 equiv.) in presence of 0.5 mM triflic acid (HOTf) or 0.5 mM Sc(OTf)₃. The formation of [Mn^{IV}(O)(dpaq)]ClO₄ (**2**) was

monitored by UV-vis spectroscopy by observing the increase in the absorption features at 700 nm and 500 nm.

Alternatively, $[\text{Mn}^{\text{IV}}(\text{O})(\text{dpaq})]\text{ClO}_4$ (**2**) was prepared by reacting a 0.5 mM $[\text{Mn}^{\text{III}}(\text{OH})(\text{dpaq})](\text{ClO}_4)$ (**1**) in acetonitrile at 293K with a mixture of $[\text{Ru}^{\text{III}}(\text{bpy})_3]^{3+}$ and HOTf (0.5 mM each in acetonitrile).

V.6.3. Kinetic measurements and product analysis

Kinetic measurements of substrate oxidations were performed at 293 K. The substrates were first added to a 2.0 mL 0.5 mM acetonitrile solutions of **2**, generated *in situ* by the addition of 1.0 equivalent of $\text{Sc}(\text{OTf})_3$ and 1.2 equivalent of *m*-CPBA. The decay of the 700 nm UV-Vis band, associated with **2**, was then monitored over time. Fitting the decay of **2** to a single-exponential function yielded pseudo-first order rate constant, k_{obs} . Second-order rate constants, k_2 ($\text{M}^{-1}\text{s}^{-1}$), were determined from the slope of a plot of k_{obs} (s^{-1}) against substrate concentration (Fig.V.15 –17).

To isolate and identify the organic products upon completion of the reaction, the reaction mixtures were filtered through a plug of silica and eluted with chloroform or ethyl acetate. The filtered solutions were then analyzed by GC-MS or GC with pentafluoridobenzene (PFIB) as the quantification standard.

V.6.4. Generation of $\text{Mn}^{\text{IV}}\text{-O}$ (**2**) with $[\text{Ru}(\text{bpy})_3]^{3+}$

The $[\text{Ru}(\text{bpy})_3](\text{ClO}_4)_2$ was prepared from $[\text{Ru}(\text{bpy})_3]\text{Cl}_2$ by following previously reported procedure [33]. The one electron oxidant $[\text{Ru}(\text{bpy})_3]^{3+}$ was from $[\text{Ru}(\text{bpy})_3](\text{ClO}_4)_2$ by oxidizing with lead dioxide prior to use in spectrophotometric experiments. A 10mM solution of $[\text{Ru}(\text{bpy})_3](\text{ClO}_4)_2$ was prepared by dissolving 38.42 mg of $[\text{Ru}(\text{bpy})_3](\text{ClO}_4)_2$ in 5mL acetonitrile containing 10mM HOTf. Excess lead dioxide was added to this mixture and stirred for 5 minutes at room temperature. The orange color solution turned bluish green in color. The final concentration of $[\text{Ru}(\text{bpy})_3]^{3+}$ and HOTf in the solution during the UV-visible spectroscopic studies was 10mM.

V.6.5. Computational Methods

Calculations at the level of Density Functional Theory (DFT) have also been performed to gain more insight into the electronic structure of the complex under investigation. The molecule is optimized with meta-hybrid TPSSh functional [17]

and relativistic basis set implemented through zeroth-order regular approximation (ZORA) [18] retaining one-center terms and using ZORA-recontracted def2-TZVP basis sets for all elements other than C and H, for which ZORA-def2-SVP basis sets were used [19]. To eliminate any potential errors from the use of resolution of identity (RI) and chain-of-spheres (COSX) approximations to coulomb and exact exchange,[29] a large decontracted SARC/J auxiliary basis set is used [30]. Increased integration accuracy (Grid6, GridX8 and IntAcc 6.0 in ORCA convention) and tight SCF convergence criteria were applied. During optimization, solvent effect is included as a dielectric medium through the conductor-like polarizable continuum model (CPCM) [31]. To obtain optical absorption spectra of the compound time dependent density functional theory (TDDFT) is employed with long-range corrected CAM-B3LYP functional [32] with all other settings unchanged as above. All the calculations are implemented in ORCA (version 4.0) [16].

V.7. References

- [1] (a) T. J. Meyer, M. H. V. Huynh, H. H. Thorp, *Angew. Chem. Int. Ed.* 2007, **46**, 5284; (b) J. J. A. Cotruvo, J. Stubbe, *Metallomics*. 2012, **4**, 1020; (c) R. H. Holm, *Chem. Rev.* 1987, **87**, 1401; (d) J. T. Groves, Y. Z. Han, in: P. R. Ortiz de Montellano (Ed.), *Cytochrome P-450. Structure, Mechanism and Biochemistry*, 2nd ed., Plenum Press, New York, 1995, pp. 3–48.
- [2] (a) J. P. McEvoy, G. W. Brudvig, *Chem. Rev.* 2006, **106**, 4455; (b) V. Krewald, M. Retegan, D. A. Pantazis, *Top. Curr. Chem.* 2015, **371**, 23; (c) N. Cox, D. A. Pantazis, F. Neese, W. Lubitz, *Acc. Chem. Res.* 2013, **46**, 1588.
- [3] A. F. Miller, *FEBS Letters*. 2012, **586**, 585.
- [4] (a) K. B. Clark, P. N. Culshaw, D. Griller, F. P. Lossing, J. A. M. Simões, J. C. Walton, *J. Org. Chem.* 1991, **56**, 5535; (b) A. F. Miller, *Curr. Opin. Chem. Biol.* 2004, **8**, 162; (c) L. E. Grove, T. C. Brunold, *Comments Inorg. Chem.* 2008, **29**, 134; (d) C. Su, E. H. Oliw, *J. Biol. Chem.* 1998, **273**, 13072; (e) C. Su, M. Sahlin, E. H. Oliw, *J. Biol. Chem.* 2000, **275**, 1883.
- [5] J. P. Layfield, S. Hammes-Schiffer, *Chem. Rev.* 2013, **114**, 3466.
- [6] M. Retegan, V. Krewald, F. Mamedov, F. Neese, W. Lubitz, N. Cox, D. A. Pantazis, *Chem. Sci.* 2016, **7**, 72.
- [7] (a) Y. Umena, K. Kawakami, J. R. Shen, N. Kamiya, *Nature*. 2011, **473**, 55; (b) M. Suga, F. Akita, K. Hirata, G. Ueno, H. Murakami, Y. Nakajima, T. Shimizu, K. Yamashita, M. Yamamoto, H. Ago, J. R. Shen, *Nature*. 2015, **517**, 99.
- [8] (a) M. M. Najafpour, G. Renger, M. Holynska, A. N. Moghaddam, E. V. Aro, R. Carpentier, H. Nishihara, J. J. Eaton-Rye, J. R. Shen, S. I. Allakhverdiev, *Chem. Rev.* 2016, **116**, 2886; (b) D. Kim, K. K. Sakimoto, D. Hong, P. Yang, *Angew. Chem. Int. Ed.* 2015, **54**, 2; (c) X. Sala, S. Maji, R. Bofill, J. Garcia-Anton, L. Escriche, A. Llobet, *Acc. Chem. Res.* 2014, **47**, 504; (d) J. D. Blakemore, R. H. Crabtree, G. W. Brudvig, *Chem. Rev.* 2015, **115**, 12974; (e) M. D. Karkas, B. Akermark, *Dalton Trans.* 2016, **45**, 14421; (f) I. Gamba, Z. Codola, J. Lloret-Fillol, M. Costas, *Coord. Chem. Rev.* 2017, **334**, 2.
- [9] Y. Nishida, Y. Morimoto, Y. M. Lee, W. Nam, S. Fukuzumi, *Inorg. Chem.* 2013, **52**, 3094.
- [10] T. Taguchi, R. Gupta, B. L. Kaiser, D. W. Boyce, V. K. Yachandra, W. B. Tolman, J. Yano, M. P. Hendrich, A. S. Borovik, *J. Am. Chem. Soc.* 2012, **134**, 1996.

- [11] (a) B. Lassalle-Kaiser, C. Hureau, D. A. Pantazis, Y. Pushkar, R. Guillot, V. K. Yachandra, J. Yano, F. Neese, E. A. Mallart, *Energy Environ Sci.* 2010, **3**, 924; (b) A. S. Borovik, *Acc. Chem. Res.* 2005, **38**, 54; (c) T. H. Parsell, R. K. Behan, M. P. Hendrich, M. T. Green, A. S. Borovik, *J. Am. Chem. Soc.* 2006, **128**, 8728; (d) T. H. Parsell, M. Y. Yang, A. S. Borovik, *J. Am. Chem. Soc.* 2009, **131**, 2762; (e) K. J. Young, M. K. Takase, G. W. Brudvig, *Inorg. Chem.* 2013, **52**, 7615.
- [12] W. A. Remers, *The Chemistry of Antitumor Antibiotics* (John Wiley, New York), 1979, **1**, 176.
- [13] G. B. Wijeratne, B. Corzine, V. W. Day, T. A. Jackson, *Inorg. Chem.* 2014, **53**, 7622.
- [14] (a) H. Yoon, Y. M. Lee, X. Wu, K. B. Cho, R. Sarangi, W. Nam, S. Fukuzumi, *J. Am. Chem. Soc.* 2013, **135**, 9186; (b) J. Chen, Y. M. Lee, K. M. Davis, X. Wu, M. S. Seo, K. B. Cho, H. Yoon, Y. J. Park, S. Fukuzumi, Y. N. Pushkar, W. Nam, *J. Am. Chem. Soc.* 2013, **135**, 6388.
- [15] M. Sankaralingam, S. H. Jeon, Y. M. Lee, M. S. Seo, K. Ohkubo, S. Fukuzumi, W. Nam, *Dalton Trans.* 2016, **45**, 376.
- [16] F. Neese, The ORCA program system. *WIREs Comput. Mol. Sci.* 2012, **2**, 73.
- [17] V. N. Staroverov, G. E. Scuseria, J. M. Tao, J. P. Perdew, *J. Chem. Phys.* 2003, **119**, 12129.
- [18] (a) E. VanLenthe, J. G. Snijders, E. J. Baerends, *J. Chem. Phys.* 1996, **105**, 6505; (b) E. Vanlenthe, E. J. Baerends, J. G. Snijders, *J. Chem. Phys.* 1994, **101**, 9783.
- [19] D. A. Pantazis, X. Y. Chen, C. R. Landis, F. Neese, *J. Chem. Theory. Comput.* 2008, **4**, 908; (b) A. Schafer, C. Huber, R. Ahlrichs, *J. Chem. Phys.* 1994, **100**, 5829.
- [20] D. F. Leto, A. A. Massie, D. B. Rice, T. A. Jackson, *J. Am. Chem. Soc.* 2016, **138**, 15413.
- [21] (a) S. Pal, P. Ghosh, A. Chakravorty, *Inorg. Chem.* 1985, **24**, 3706; (b) D. P. Kessissoglou, X. Li, W. M. Butler, V. L. Pecoraro, *Inorg. Chem.* 1987, **26**, 2487; (c) T. Weyhermüller, T. K. Paine, E. Bothe, E. Bill, P. Chaudhuri, *Inorg. Chim. Acta.* 2002, **337**, 344; (d) T. M. Rajendiran, J. W. Kampf, V. L. Pecoraro, *Inorg. Chim. Acta.* 2002, **339**, 497.
- [22] S. Stoll, A. Schweiger, EasySpin, *J. Magn. Reson.* 2006, **178**, 42.

- [23] M. Zlatař, M. Gruden, O. Y. Vassilyeva, E. A. Buvaylo, A. N. Ponomarev, S. A. Zvyagin, J. Wosnitza, J. Krzystek, P. G. -Fernandez, C. Duboc, *Inorg. Chem.* 2016, **55**, 1192.
- [24] S. C. Sawant; X. Wu, J. Cho, K. B. Cho, S. H. Kim, M. S. Seo, Y. M. Lee, M. Kubo, T. Ogura, S. Shaik, W. Nam, *Angew. Chem. Int. Ed.* 2010, **49**, 8190.
- [25] I. Garcia-Bosch, A. Company, C. W. Cady, S. Styring, W. R. Browne, X. Ribas, M. Costas, *Angew. Chem.* 2011, **123**, 5766.
- [26] J. Chen, K.-B. Cho, Y.-M. Lee, Y. H. Kwon, W. Nam, *Chem. Commun.* 2015, **51**, 13094.
- [27] G. Yin, A. M. Danby, D. Kitko, J. D. Carter, W. M. Scheper, D. H. Busch, *J. Am. Chem. Soc.* 2008, **130**, 16245.
- [28] Y. Hitomi, K. Arakawa, T. Funabiki, M. Kodera, *Angew. Chem. Int. Ed.* 2012, **51**, 3448.
- [29] F. Neese, F. Wennmohs, A. Hansen, U. Becker, *Chem. Phys.* 2009, **356**, 98.
- [30] (a) F. Weigend, *Phys. Chem. Chem. Phys.* 2006, **8**, 1057; (b) E. M. Sproviero, J. A. Gascón, J. P. McEvoy, G. W. Brudvig, V. S. Batista, *J. Am. Chem. Soc.* 2008, **130**, 3428.
- [31] (a) M. Cossi, N. Rega, G. Scalmani, V. Barone, *J. Comput. Chem.* 2003, **24**, 669; (b) V. Barone, M. Cossi, *J. Phys. Chem. A.* 1998, **102**, 1995.
- [32] T. Yanai, D. P. Tew, N. C. Handy, *Chem. Phys. Lett.* 2004, **393**, 51.
- [33] G. P. McDermott, P. Jones, N. W. Barnett, D. N. Donaldson, P. S. Francis, *Anal. Chem.* 2011, **83**, 5453.